Quantifying the impact of operating temperature on cracking in battery electrodes, using super-resolution of microscopy images and stereology

Orkun Furat[1,*], Donal P. Finegan[2,*], Zhenzhen Yang[3], Matthias Neumann[1], Sangwook Kim[4], Tanvir R. Tanim[4], Peter Weddle[2], Kandler Smith[2], Volker Schmidt[1]

[1] *Institute of Stochastics, Ulm University, Helmholtzstraße 18, 89069 Ulm, Germany*
[2] *National Renewable Energy Laboratory, 15013 Denver W Parkway, Golden, CO 80401, USA*
[3] *Chemical Sciences and Engineering Division, Argonne National Laboratory, 9700 S. Cass Avenue, Lemont, IL 60439, USA*
[4] *Idaho National Laboratory, 2525 N. Fremont, Idaho Falls, ID 83415, USA*

Abstract

There are numerous factors that can have an impact on the degradation behavior of batteries, such as the number of recharge cycles or the charge rate. Here, we investigate the influence of operating temperature on the structural degradation of the microstructure in lithium-ion positive electrodes. For that purpose, the microstructure is characterized for cathodes which have been cycled for 200 cycles under 6C (10-minute) charging at different operating temperatures, namely, 20 °C, 30 °C, 40 °C, and 50 °C. For each operating condition scanning electron microscopy (SEM) images of cross-sectioned $Li_xNi_{0.5}Mn_{0.3}Co_{0.2}O_2$ (NMC532) electrodes have been analyzed, to determine structural descriptors such as global particle porosity, crack size/length/width distribution, and porosity and specific surface area distribution of individual particles. Additionally, a stereological method has been deployed to investigate the local particle porosity as a function of distance to the particle center. Results show that particle porosity increases with increasing cycling temperature. Particle porosity is greatest at the particle center and decreases along the particle radius to the exterior. Particle surface area is similar across the four cycling-temperature aging conditions.

Keywords:—Lithium-ion battery, crack evolution, operating temperature, statistical image analysis, super-resolution.

1 Introduction

Structural degeneration of polycrystalline cathode materials is one mechanism that limits the lifetime of lithium-ion batteries, particularly when the batteries are fast charged [1, 2]. Quantitative analysis of microstructure images aids the understanding of degradation physics of Li-ion batteries and provides data to validate electrochemo-mechanical degradation models [3]. For the structural characterization of a material's microstructure, imaging techniques such as micro/nano computed tomography (CT) or focus-ion-beam (FIB)-based methods are quite valuable [4, 5]. In addition to aggregated quantities, such as volume fractions of phases or the porosity of the material, image data acquired with such techniques allows the determination of more advanced structural descriptors that provide a much more detailed insight into the microstructure. For example, from image data of particulate materials (e.g., cathode materials), individual particles can be identified, descriptors for their size and shape can be computed, as well as the (joint) distribution of such descriptors [6, 7]. This kind of advanced quantitative structural characterization of a material's microstructure has numerous advantages. For example, the structural descriptors can be correlated with other parameters (e.g., effective macroscopic properties, or operating parameters), in order to quantify, for example, microstructure-property relationships or the influence of operating parameters on the microstructure [8, 9].

*Corresponding authors
Email addresses: orkun.furat@uni-ulm.de (Orkun Furat), donal.finegan@nrel.gov (Donal P. Finegan)

Additionally, the structural characterization of experimentally acquired images can be utilized to tune unknown parameters in physical models for the numerical simulation of macroscopic properties [10].

Note that 3D imaging techniques (e.g., CT) can be quite expensive in both time and resources for the structural characterization of a material's microstructure. Therefore, often 2D imaging techniques like scanning electron microscopy (SEM) are considered which can provide highly resolved image data of planar sections through the material. However, the quantitative analysis of 3D morphologies based on such 2D image data can be difficult. For example, disks observed in planar sections through spherical particles exhibit smaller diameters, i.e., the diameter distribution of observed disks does not coincide with the diameter distribution of the spheres [11, 12]. Such discrepancies can be corrected with methods from stereology. The field of stereology deals with the determination of geometrical properties of 3D structures from lower-dimensional observations, e.g., planar sections [13]. There are various results concerned with estimating aggregated descriptors such as volume fractions or specific surface areas of multi-phase materials from planar sections [13,14]. Additionally, there are numerous results concerned with the estimation of the average volume, surface area etc. of convex particles [15]. However, the computation of a particle size distribution from planar sections is more difficult. Some theoretical results are available for spherical particles [14], which allow for the estimation of the radius distribution of spherical particles from observed circular cross-sections. For more general shapes such an estimation procedure can become more difficult. Thus, more restrictions on the geometry of the particles or their distribution have to be made. For example, in general it is not possible to estimate the joint distribution of size and shape of ellipsoids from planar sections [16,17]. However, by introducing further constraints, e.g., by considering ellipsoids with a fixed shape, the size distribution can be estimated from planar sections [12]. In [18, 19] methods have been presented to estimate the size distribution of star-shaped particles from planar sections through a known reference point of a particle, assuming a parametric representation for the distribution of the particle geometry. Additionally, there are data-driven methods, which rely on the simulation of virtual particle geometries and of their planar sections in order to correlate planar sections of particles with descriptors for the 3D shape [20] or, in the case of composite particles, with descriptors for the volume fractions of phases [21]. For some examples, in which such techniques are deployed to investigate 3D structural properties of battery materials from planar sections the reader is referred to [22–25].

In the present paper, we follow the method laid out in [8] for the characterization of the microstructure of lithium-ion positive electrodes which have been cycled under various operating temperatures and imaged in planar sections. While previous work has demonstrated quantification of cracks with cycling and temperature [26], here we focus our quantitative analysis on the use of SEM data alone, making the approach accessible to most industry and academic research labs. Furthermore, we make a quantitative correlation between crack evolution and loss of active material in the positive electrode. A schematic visualization of the workflow described in the present paper is given in Figure 1. For the structural characterization of cycled cathodes, SEM image data of cross-sectioned $LiNi_{1-x-y}Mn_yCo_xO_2$ (NMC) cathodes is considered. A cutout from such an SEM image is shown in Figure 1(top row, center). Since there is a trade-off between field of view (FOV) and resolution in many imaging techniques, i.e., for SEM images with a large FOV which depict numerous cathode particles it may be difficult to identify fine features such as cracks within particles. Since, however, cracks are an indicator for the structural degradation of cathodes, we pre-process the images in order to increase their resolution, making crack identification easier. More precisely, in a first step a super-resolution technique is deployed in order to artificially increase the resolution of SEM images, see Figure 1(top row, right) [27]. Then, the super-resolved image data is segmented in order to enable a quantitative characterization. More precisely, three different kinds of segmentations are considered in the present paper: (i) a phase-wise segmentation which allows the distinction between background, solid and crack phase, see Figure 1(second row, right). From a phase-wise segmentation, we can compute aggregated descriptors of cycled cathodes, such as the global particle porosity, which quantifies the overall amount of cracks. Additionally, the results obtained in (i) are the basis for the computation of instance segmentations, i.e., (ii) a crack-wise segmentation and a (iii) particle-wise segmentation. More precisely, from the results obtained (ii) individual cracks can be identified, see Figure 1(second row, center), thus, allowing for the computation of morphological descriptors (size, length and width) for each observed crack. Such descriptors (or their distribution) allow for a more in-depth investigation of the influence of cycling conditions on structural degradation [8]. Similarly to (ii), in (iii) individual particles can be identified, see Figure 1(second row, left). By combining the particle-wise segmentation with the phase-wise segmentation (which provides the information on the location of cracks) even further descriptors like the porosity of individual particles can be determined.

Furthermore, we present a method with which we compute the local particle porosity as a function of distance

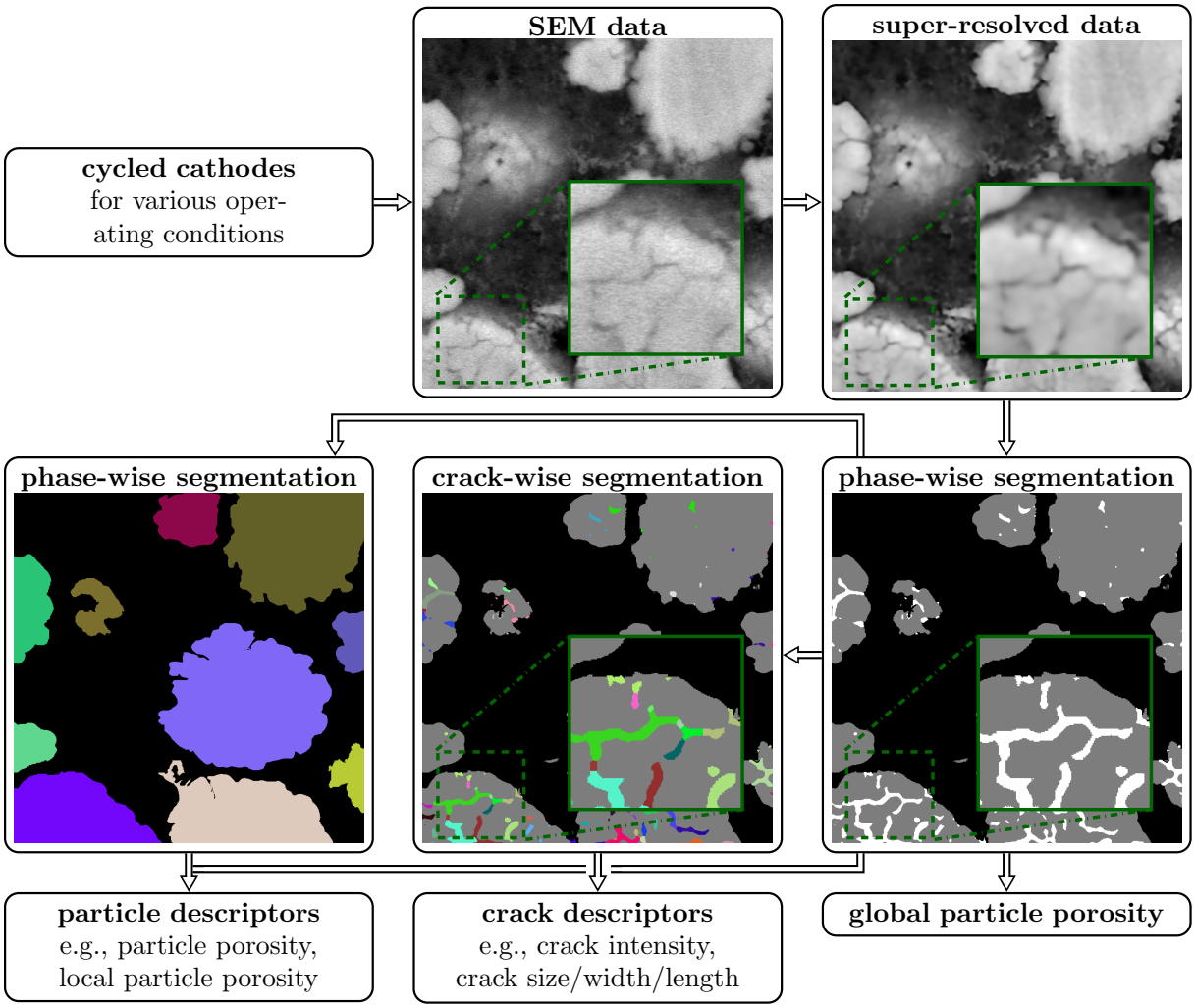

Figure 1: Workflow for the characterization of cycled cathodes. First, SEM image data (top row, center) of cathodes cycled under various operating temperatures is super-resolved (top row, right), using a generative adversarial network. The dashed green squares are visualized with a magnification of 2 within the green solid-lined squares. From the super-resolved data a phase-wise segmentation (second row, right) is determined, using a convolutional neural network. This allows the distinction between background (black), solid (gray) and crack phase (white). By applying conventional image processing techniques (namely the watershed transformation), a crack-wise segmentation (second row, center) can be determined within the crack phase, such that individual cracks are identified. For visualization purposes, the solid phase is depicted in gray. Additionally, a particle-wise segmentation (second row, left) can be computed for the union of the solid and crack phases, such that individual particles can be identified. Note that small particles have been removed from the subsequent analysis. Finally, from these three segmentations various descriptors are determined which quantify the structural degradation (bottom row).

to the particle center from the particle- and phase-wise segmentation, see Figure 1(bottom row, left). Note that this is a non-trivial problem, because only cross-sections of the nearly spherical NMC particles with dispersed sizes are visible in the SEM image data, i.e., it is unclear at which height the cross-section is located with respect to the particle center, making it impossible to determine the exact distance of a point within the cross-section to the particle center. In order to overcome this issue, we deploy methods from stereology to estimate such distances from cross-sectioned image data [14].

The paper is organized as follows. Section 2 describes the workflow depicted in Figure 1 in detail, i.e., the battery cell construction, electrochemical aging tests, post-mortem SEM imaging, followed by image data processing steps, namely super-resolution, and phase/crack/particle segmentation approach. We define a number of morphological descriptors of the cracked particles that are presented in Section 3. Moreover, Section 4 hypothesizes how the morphological observations relate to electrochemical degradation. Section 5 concludes.

2 Methods

2.1 Electrochemical aging test and data analysis

In this section, we describe the cycling experiments performed for aging cathodes under various operating temperatures. For that purpose, eight single-layer pouch cells (xx3450 format) were built by Cell Analysis, Modeling, and Prototyping (CAMP) Facility and tested by Electrochemical Analysis and Diagnostics Laboratory Facility (EADL) at Argonne National Laboratory (ANL). The cathodes are composed of 90 wt% $Li(Ni_{0.5}Mn_{0.3}Co_{0.2})O_2$, 5 wt% Timcal C45 carbon and 5 wt% of the binder Solvay 5130 PVDF. Details and the composition of the anode can be found in [28]. The cells were pre-formed by charging them at a rate of C/10 with a 1.5 V tap charge at a temperature of 30 °C. This charge was maintained for 15 minutes before a 12-hour open-circuit voltage (OCV) relaxation period was allowed. After this period, the cells were subjected to three cycles of charging between 3 V and 4.1 V using a constant-current, constant-voltage (CCCV) charge profile. During charging, the C/10 rate was maintained until the potential reached 4.1 V and then held until the current was below the C/20 rate. The constant-current (CC) discharge cycle was performed at a rate of C/10 to 3 V. The CCCV profile was repeated for three additional cycles by charging at the C/2 rate until the current fell below C/10 and discharging at the C/2 rate. Finally, the cells were charged at the C/10 rate to 3.5 V and held at that potential for 6 hours to put them in a safe state. The cells were then degassed and vacuum sealed. Extreme Fast Charge (XFC) Cycling (Maccor 4000 series) was performed in thermally controlled chambers (Tenny Environmental) at 20, 30, 40, and 50 °C. The post-formation capacity tests at C/20 resulted in 35.5 mAh capacity with less than 1.5 % 1σ variability. Two cells at each temperature were aged under a fast-charge protocol at 6C constant-current charge to 4.1 V, followed by 4.1 V constant-voltage hold until 10-minutes total charge time had elapsed. After each charge, the cells were relaxed for 15 min, which followed by a C/2 discharge to 3 V. Another 15 min rest was added before the next charge step. Cycling was paused at every 25 cycling intervals to perform Reference performance tests (RPT) that included C/20 capacity, HPPC test and electrochemical impedance spectroscopy tests (Solartron). More detail about cell build and testing procedure can be found in [28].

2.2 SEM analysis

In order to investigate the structural degradation of cycled cathodes for the different operating conditions, SEM image data is acquired, see Figure 1(top row, center). More precisely, after 200 aging cycles, the cells were torn down in an argon-atmosphere glove box with 0.1 ppm oxygen and 0.2 ppm water. The cycled cathodes were cut into $1\times1\,cm^2$ pieces and loaded on the holder for the cross-sectional preparation. The samples were polished with a 4 kV Ar^+ ion beam for 4 hours inside of a cross-sectional polisher (JEOL CP19520). The cross-sectioned samples were directly imaged utilizing a JEOL JSM-6610LV scanning electron microscopy (SEM) equipment. Both high- and low-resolution images of the samples have been acquired with pixel sizes of approximately 14.3 nm and 38.5 nm, respectively.

2.3 Data preprocessing

A quantitative characterization of structural degradation in cycled cathodes cannot be performed directly from the SEM image data the acquisition of which has been described in Section 2.2. For that purpose, we now explain the image processing steps performed on the SEM image data of differently cycled cathodes to quantitatively analyze the crack formation in NMC particles. Note that the methods described in this section are a modification of the procedure which we used in a previous paper, see [8]. More precisely, this section deals with various types of segmentation of the SEM images which are formally defined as a mapping $I\colon W \to [0,1]$, where the set W of pixels is given by $W = \{1,\dots,w\} \times \{1,\dots,h\}$ with image width $w > 0$ and image height $h > 0$.

The first type of segmentation is the phase-wise segmentation $S\colon W \to \{0,1,2\}$ of I which assigns each pixel to the solid phase, the crack phase of particles or to the background. More precisely, such a phase-wise segmentation is of the form

$$S(x) = \begin{cases} 1, & \text{if } x \text{ corresponds to the solid phase of a particle,} \\ 2, & \text{if } x \text{ corresponds to the crack phase of a particle,} \\ 0, & \text{else,} \end{cases} \tag{1}$$

for each pixel $x \in W$, see Figure 1(second row, right), where pixel values 0, 1, 2 are visualized in black, gray and white, respectively. Details regarding the computation of phase-wise segmentations are given below. From a phase-wise segmentation, aggregated descriptors such as the total area of phases or their fractions (e.g., the global particle porosity) can be computed which quantify the overall degree of structural degradation of NMC particles. However, phase-wise segmentations do not allow us to identify individual cracks in the image data, which would be necessary to investigate more detailed descriptors, e.g., the length of individual cracks or even the crack length distribution. Therefore, later on, we additionally identify individual cracks in the segmented images S by partitioning the crack phase $\{x \in W : S(x) = 2\}$ into $n_\mathrm{c} > 0$ sets of pixels associated with individual cracks. More precisely, the crack-wise segmentation $S_\mathrm{c}\colon W \to \{0,1,\dots,n_\mathrm{c}\}$ is given by

$$S_\mathrm{c}(x) = \begin{cases} i, & \text{if } x \text{ belongs to the } i\text{-th crack,} \\ 0, & \text{else,} \end{cases} \tag{2}$$

where the sets $\{x \in W\colon S_\mathrm{c}(x) = 2\}$ and $\{x \in W\colon S_\mathrm{c}(x) > 0\}$ have to be equal to ensure that the crack-wise segmentation is a partitioning of the crack phase. Such a crack-wise segmentation of the crack phase is shown in Figure 1(second row, center), where each identified crack is visualized in a randomly chosen color (for visualization purposes, the solid phase is still shown in gray). The crack-wise segmentation can be used to determine crack descriptors such as crack size, width and length for individual cracks and to investigate their probability distribution, see Section 2.4. Such descriptors provide more detailed information on the structural degradation of cathodes than the global particle porosity—allowing for a more comprehensive investigation of the influence of operating conditions on the structural degradation of cathodes.

Note that both the phase-wise and the crack-wise segmentations do not allow for the identification of individual NMC particles in the SEM data. However, this would allow for further options for the quantitative characterization of the structural degradation, e.g., the computation of the porosity of individual particles and even their distribution. In order to enable the computation of such particle-related descriptors, we then determine particle-wise segmentations of the segmented images S by partitioning the union set $\{x \in W\colon S(x) = 1\} \cup \{x \in W\colon S(x) = 2\} = \{x \in W\colon S(x) > 0\}$ of the particle and crack phases into $n_\mathrm{p} > 0$ sets of pixels associated with individual particles. Such a particle-wise segmentation $S_\mathrm{p}\colon W \to \{0,1,\dots,n_\mathrm{p}\}$ is given by

$$S_\mathrm{p}(x) = \begin{cases} i, & \text{if } x \text{ belongs to the } i\text{-th particle or to the crack phase within the } i\text{-th particle,} \\ 0, & \text{else,} \end{cases} \tag{3}$$

such that $\{x \in W\colon S_\mathrm{p}(x) > 0\}$. Such a particle-wise segmentation is shown in Figure 1(second row, left), where each identified particle is visualized in a randomly chosen color. Then, from the particle-wise segmentation S_p we can determine a porosity value for each particle and, thus, the probability distribution of particle porosities, see Section 2.4.

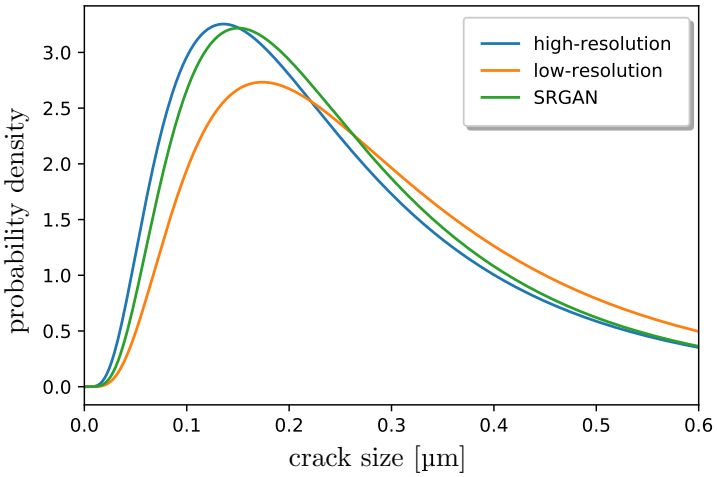

Figure 2: Performance of super-resolution. Probability densities of the crack size determined from segmented low- (orange) and high-resolution SEM-image data considered in [27]. After super-resolving the low-resolution image data, the resulting probability density (green) exhibits a better agreement with the corresponding distribution determined from high-resolution data. This figure is adapted from Fig. 5a in [27] and is licensed under CC BY 4.0 `https://creativecommons.org/licenses/by/4.0/`.

2.3.1 Super-resolution

Before the phase-wise segmentation is performed, recall that in Section 2.2 both low- and high-resolution SEM images have been acquired. In comparison to the low-resolution images, in high-resolution images fine features such as cracks are more clearly visible—thus, making the task of computing a phase-wise segmentation easier. However, due to the small FOV in high-resolution images only a few particles (≈ 10) are visible, whereas in low-resolution images the number of observable particles is (on average) increased by a factor of $(38.5\,\mathrm{nm}/14.3\,\mathrm{nm})^2 \approx 7.29$. Thus, low-resolution images are statistically more representative which is, however, accompanied with a more difficult task for the computation of a phase-wise segmentation. In order to leverage the advantages of both resolutions, we train a neural network to perform super-resolution, i.e., to artificially increase the resolution of low-resolution images—resulting in the same resolution as in high-resolution images while remaining the original FOV [29]. It has been shown in [27] that for similar SEM data of cracked cathodes, super-resolution performed by a generative adversarial network (GAN) (namely, an SRGAN) can improve segmentation results significantly, see Figure 2.

Therefore, we train an SRGAN [27, 29] to perform super-resolution on the low-resolution image data considered in the present paper, see Figure 1(top row, right). An SRGAN is comprised of two neural networks, namely, a so-called generator G_{θ_G} and a discriminator D_{θ_D}, where θ_G and θ_D denote the trainable parameters with values in some parameter spaces Θ_G and Θ_D, respectively. The architectures of the two neural networks are visualized in Figure 3. The task in training the generator G_{θ_G}, see Figure 3a, is to calibrate its trainable parameters such that the output $\widehat{I} = G_{\theta_\mathrm{G}}(I_\mathrm{low})$ for some low-resolution image I_low resembles a highly resolved version I_high. Note that the upsampling layer of the generator increases the resolution of the input image by a factor of $\frac{1}{2} \cdot \frac{35}{13}$ followed by an additional increase in resolution by a factor of 2 by the pixelshuffle layer. Thus, the generator increases the resolution of an input image by a factor of $\frac{35}{13}$ which coincides with the fraction of pixel sizes $s_1 \approx 14.3\,\mathrm{nm}$ and $s_2 \approx 38.5\,\mathrm{nm}$ of the high- and low-resolution images, respectively. The other neural network, namely, the discriminator D_{θ_D}, which takes values in the interval $(0, 1)$, is trained to distinguish between I_high and $\widehat{I}$. More precisely, the discriminator should return values close to 1 when the input is a high-resolution image I_high, whereas for a super-resolved image $\widehat{I}$ the discriminator's output should be close to 0. On the other hand, with respect to the generator G_{θ_G}, it is preferable to create super-resolved versions $\widehat{I}$ of I_low for which $D_{\theta_\mathrm{D}}(\widehat{I})$ is closed to 1. This can be formulated as a minimax problem, given by

$$\min_{\theta_\mathrm{G}\in\Theta_\mathrm{G}} \max_{\theta_\mathrm{D}\in\Theta_\mathrm{D}} \mathbb{E}\left[\mathrm{PL}(G_{\theta_\mathrm{G}}(J_\mathrm{low}), J_\mathrm{high})\right] + 2\left(\mathbb{E}\left[\log D_{\theta_\mathrm{D}}(J_\mathrm{high})\right]\mathbb{E}\left[\log\left(1 - D_{\theta_\mathrm{D}}(G_{\theta_\mathrm{G}}(J_\mathrm{low}))\right)\right]\right), \tag{4}$$

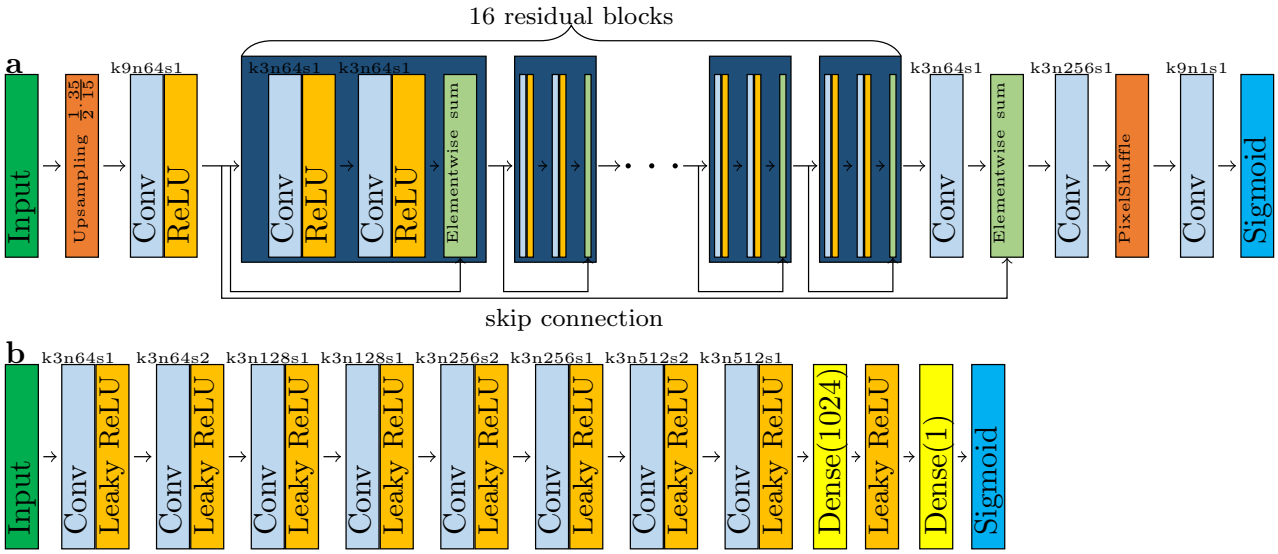

Figure 3: SRGAN. Architectures of the generator (a) and discriminator (b) used for performing super resolution. The numbers above convolutional layers, denoted by Conv, indicate the kernel size, the number of feature maps and the stride, e.g., k9n64s1 indicates a layer with kernel size 9, 64 feature maps and a stride of 1. This figure is adapted from Fig. 1 in [27] and is licensed under CC BY 4.0 `https://creativecommons.org/licenses/by/4.0/`.

where J_{low} is a cutout (with a size of 96×96 pixels) taken at random from a randomly chosen low-resolution image and J_{high} is the corresponding highly resolved version of J_{low} [27]. Furthermore, the function PL is referred to as perceptual loss which measures the discrepancy between J_{high} and the super-resolved image $G_{\theta_{\text{G}}}(J_{\text{low}})$ [29]. More precisely, the perceptual loss $\text{PL}(I_1, I_2)$ between two images I_1, I_2 is given by

$$\text{PL}(I_1, I_2) = \text{MSE}(\text{VGG}(I_1), \text{VGG}(I_2)), \tag{5}$$

where MSE is the mean squared error and VGG denotes the 2nd convolutional layer before the 2nd maxpooling layer of the Visual Geometry Group network with depth 19 [30]. Note that instead of considering the perceptual loss $\text{PL}(G_{\theta_{\text{G}}}(J_{\text{low}}), J_{\text{high}})$, the discrepancy between high-resolution and super-resolved images could be measured by the mean squared error, i.e., using $\text{MSE}(G_{\theta_{\text{G}}}(J_{\text{low}}), J_{\text{high}})$. However, in [29] it was shown that the use of the perceptual loss PL leads to a better performance in super-resolution tasks.

We have implemented the SRGAN architecture in the Python package TensorFlow [31] and trained the generator $G_{\theta_{\text{G}}}$ and discriminator $D_{\theta_{\text{D}}}$ alternately using the stochastic gradient-descent method Adam [32] with a learning rate of 10^{-4} and a batch size of 32, i.e., in each training step the expected values in Formula (4) and their gradients with respect to the trainable parameters $\theta_{\text{G}}, \theta_{\text{D}}$ are estimated by means of Monte Carlo simulation. The training data, i.e., the pairs of low- and high-resolution images from which random cutouts are taken during training consists of 15 pairs. Note that after 20 consecutive training steps the performance of the GAN is evaluated using a validation loss. More precisely, the validation loss is given by the perceptual loss PL on 92 random pairs of cutouts taken from a validation dataset consisting of three pairs of low- and high-resolution images. Training is terminated if the validation loss does not improve within 10 such consecutive performance checks. Then, the trainable parameters θ_{G} and θ_{D} are reset to the ones for which the validation loss has been smallest, resulting in the trained generator denoted by G.

After training, the network is deployed to all low-resolution images of cracked cathodes to obtain high-resolution versions, which we denote by $I\colon W = \{1, \ldots, 5972\} \times \{1, \ldots, 4478\}$ from here on, see Figure 4. Now that high-resolution SEM images are available, which makes the identification of cracks easier, while still having a relatively large FOV, we can turn our attention to the computational details for the phase-, crack- and particle-wise segmentations.

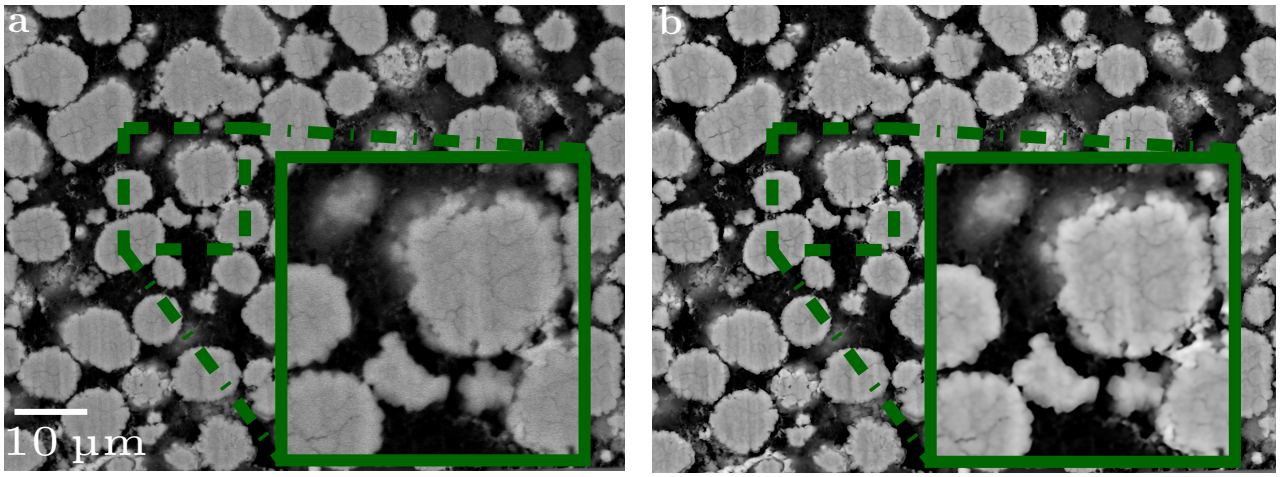

Figure 4: Super-resolution. SEM image (a) and corresponding super-resolved image (b). The dashed green squares are visualized with a magnification of 2.5 within the green solid-lined squares. All figures use the same length scales.

2.3.2 Phase- and crack-wise segmentation

For determining a phase-wise segmentation $S\colon W \to \{0,1,2\}$ of a super-resolved image I which satisfies Equation (1), see also Figure 1 (second row, right), we deploy the method described in [8]. More precisely, we train a convolutional neural network, namely a modular U-net [33] with U-depth of 5 and 32 filters in the first convolutional layer. Note that the U-depth influences the receptive field of the U-net. In comparison, the original architecture described in [34] has a lower U-depth of 4. The increased value of 5 for the U-depth parameter is chosen to increase the receptive field of the considered U-net which is necessary due to the relatively large resolution of the super-resolved image data. Additionally, we increase the receptive field by setting the dilation factor of the convolutional layers to 4. In order to ensure that the network's output has the same dimensions as the input image, the padding option of all convolutional layers is set to SAME. Since the task of the U-net is to classify for a super-resolved image I whether a pixel $x \in W$ is associated with either background, solid or crack phase, the output layer has three channels with the softmax function as activation function. This ensures that the output for some super-resolved image I is a three-channel image $\widehat{Y}\colon W \times \{1,2,3\} \to [0,1]$ with $\widehat{Y}(x,1) + \widehat{Y}(x,2) + \widehat{Y}(x,3) = 1$ for each pixel $x \in W$, i.e., the values $\widehat{Y}(x,1), \widehat{Y}(x,2), \widehat{Y}(x,3)$ can be interpreted as the network's certainty that the pixel x is located within the background, particle or crack phase, respectively. Similarly to the SRGAN considered above, the U-net is trained using the stochastic gradient-descent algorithm Adam with a learning rate of 10^{-4}, where we choose the weighted categorical cross entropy as loss function, see [8] for further details. The training and validation data consists of 3 and 1 manually annotated images , i.e., pairs of images (I, Y), where $Y\colon W \times \{1,2,3\} \to \{0,1\}$ with $Y(x,1) + Y(x,2) + Y(x,3) = 1$ for each pixel $x \in W$. Note that such a manually annotated image can be considered to be a phase-wise segmentation $S_{\text{manual}}\colon W \to \{0,1,2\}$ given by

$$S_{\text{manual}}(x) = \begin{cases} 0, & \text{if } Y(x,1) = 1, \\ 1, & \text{if } Y(x,2) = 1, \\ 2, & \text{if } Y(x,3) = 1, \end{cases} \tag{6}$$

for each $x \in W$. During training, cutouts from a randomly chosen pair (I, Y) of the training data with a size of 1024×1024 pixels are taken at random at each training step (i.e., we have a batch size of 1). After 200 consecutive training steps, the validation loss is determined by computing the weighted categorical cross entropy for 50 pairs of randomly chosen cutouts from the validation data. Similarly to the validation procedure described above, training is terminated if the validation loss does not improve in 10 consecutive performance checks.

After training, the U-net is deployed on all super-resolved images I. As mentioned above, the outputs are three-channel images $\widehat{Y}\colon W \times \{1,2,3\} \to [0,1]$, for which the values $\widehat{Y}(x,1), \widehat{Y}(x,2), \widehat{Y}(x,3)$ can be interpreted as the network's certainty that the pixel x is located within the background, particle or crack phase, respectively. This type of "fuzzy" segmentation has to be processed to obtain an image which fulfills our definition of a phase-wise

segmentation provided in Equation (1). More precisely, a phase-wise segmentation $S\colon W \to \{0,1,2\}$ is obtained from the network's output $\widehat{Y}$ by

$$S(x) = \begin{cases} 2, & \text{if } \widehat{Y}(x,3) \geq t, \\ 1, & \text{if } \widehat{Y}(x,3) < t \text{ and } \widehat{Y}(x,2) \geq \widehat{Y}(x,1), \\ 0, & \text{else,} \end{cases} \tag{7}$$

for each $x \in W$, where $t > 0$ denotes some threshold. This threshold is chosen such that the resulting segmentations have a maximal accuracy, where the manual annotations S_{manual} serve as reference.

From the phase-wise segmentation S we compute a crack-wise segmentation $S_{\text{c}}\colon W \to \{0,1,\ldots,n_{\text{c}}\}$ which satisfies Equation (2), where we deploy the segmentation procedure described in [8], see Figure 1(second row, center). More precisely, we skeletonize the crack phase $\{x \in W : S(x) = 2\}$ such that we obtain $n_{\text{c}} > 0$ discretized curves $L_1,\ldots,L_{n_{\text{c}}} \subset W$, where each curve represents an individual crack [35]. However, this set of curves is not yet a partitioning of the crack phase, i.e., a crack-wise segmentation. In order to determine the crack-wise segmentation S_{c}, we assign each pixel $x \in \{x \in W\colon S_{\text{c}}(x) = 2\}$ of the crack phase to its closest curve, i.e., $S_{\text{c}}(x) = i$ if x is closer to L_i than to L_j for each pair (i,j) with $j = 1,\ldots,i-1,i+1,\ldots,n_{\text{c}}$.

Note that such a crack-wise segmentation computed from 2D data might not be representative of the actual 3D microstructure of the cathode. For example, two cracks which are not connected in a planar section might actually be connected in 3D. Nevertheless, the structural descriptors given in Section 2.4 allow us to quantitatively compare the microstructure of the differently cycled cathode materials.

2.3.3 Particle-wise segmentation

From the phase- and crack-wise segmentations the direct computation of descriptors which characterize individual particles (e.g., particle porosity) is not possible. For that purpose, we determine a particle-wise segmentation $S_{\text{p}}\colon W \to \{0,1,\ldots,n_{\text{p}}\}$ of I, which satisfies Equation (3), see Figure 1(second row, left). More precisely, we use a marker-based watershed transformation [36], which can be considered as a type of region-growth algorithm that can partition, for example, binary images of particle systems into individual particles. Therefore, we determine a binary image $B\colon W \to \{0,1\}$ of the union of the particle and crack phases, i.e.,

$$B(x) = \begin{cases} 1, & \text{if } S(x) = 1 \text{ or } S(x) = 2, \\ 0, & \text{else.} \end{cases} \tag{8}$$

From the binary image B we determine a marker image $M\colon W \to \{0,1\}$ which is a binary image such that each connected component corresponds to an individual particle. The connected regions of the marker image provide the regions at which the region growth performed by the watershed algorithm is started. However, since particles are touching each other in B, i.e., connected components can correspond to multiple particles, B is not suited as a marker image. In order to separate the connected components of multiple particles, we perform a morphological operation, called erosion, to obtain an image with smaller but separated components. For that purpose, we compute the Euclidean distance transform $D\colon W \to [0,\infty)$ of B which is given by

$$D(x) = \begin{cases} \min\{\|x-y\|\colon y \in W, B(y) = 0\}, & \text{if } B(x) = 1, \\ 0, & \text{else,} \end{cases} \tag{9}$$

for each $x \in W$, where $\|\cdot\|$ denotes the Euclidean norm. The Euclidean distance transform D given in Equation (9) assigns to each pixel $x \in W$ its distance to the background phase. Then, we determine the eroded image M of B by thresholding D, i.e., M is given by

$$M(x) = \begin{cases} 1, & \text{if } D(x) \geq r, \\ 0, & \text{else,} \end{cases} \tag{10}$$

for each $x \in W$, where we set $r = 50$. The particle-wise segmentation $S_{\text{p}}\colon W \to \{0,1,\ldots,n_{\text{p}}\}$ is computed by means of the `watershed` function of the Python package scikit-image where $-D$ is the input image and M acts as marker image [37].

2.4 Morphological descriptors of phase-, crack- and particle-wise segmentations

In this section, we consider various morphological descriptors which characterize the structural degradation of differently aged cathodes, using the phase-, crack- and particle-wise segmentations S, S_c, S_p of super-resolved SEM images I introduced in Section 2.3, see Figure 1(bottom row). By means of these descriptors, we can quantitatively investigate the influence of battery cycling conditions on the structural degradation. In particular, we explain the computation of the morphological descriptors considered in this paper for cathodes which have been cycled at 20 °C—for the other three operating temperatures the computation of morphological descriptors is performed analogously.

Therefore, let $m = 12$ be the number of SEM images $I^{(1)}, \dots, I^{(m)}$ acquired for cathodes cycled at 20 °C. Furthermore, let $S^{(i)}, S_\mathrm{c}^{(i)}, S_\mathrm{p}^{(i)}$ denote the phase-, crack- and particle-wise segmentations of $I^{(i)}$ for $i = 1, \dots, m$. Moreover, let $n_\mathrm{c}^{(i)} > 0$ denote the number of segmented cracks in the crack-wise segmentation $S_\mathrm{p}^{(i)}$ for $i = 1, \dots, m$. Analogously, let $n_\mathrm{p}^{(i)} > 0$ denote the number of segmented particles $P_1^{(i)}, \dots, P_{n_\mathrm{p}^{(i)}}^{(i)} \subset W$ in the particle-wise segmentation $S_\mathrm{p}^{(i)}$ for $i = 1, \dots, m$.

2.4.1 Global particle porosity and crack intensity

In order to characterize the overall amount of cracks, we determine the global particle porosity $\rho \in [0, 1]$ by dividing the area of the crack phase by the area of the union of the crack and particle phases observed in the phase-wise segmentations $S^{(1)}, \dots, S^{(m)}$. More precisely, we compute such areas by counting the number of pixels associated with the corresponding phases, i.e., the global particle porosity ρ is given by

$$\rho = \frac{\sum_{i=1}^{m} \#\{x \in W \colon S^{(i)}(x) = 2\}}{\sum_{i=1}^{m} \#\{x \in W \colon S^{(i)}(x) > 0\}}, \tag{11}$$

where # denotes the cardinality of a set [8]. Note that the area fraction ρ considered in Equation (11) has been determined from a planar section of the 3D microstructure is. Under certain assumptions, ρ is an unbiased estimator for the volume fraction of cracks in the non-background phase, see [13] for further details.

Note that the quantity ρ considered in Equation (11) is the porosity of the union set of all cathode particles observed in the SEM images $S^{(1)}, \dots, S^{(m)}$, in contrast to the porosity ρ_p of individual particles considered below. The global particle porosity ρ is an aggregated descriptor which characterizes the (normalized) area associated with cracks. Another aggregated descriptor is the crack intensity λ which characterizes the frequency of cracks. More precisely, it is given by the number of cracks per area unit of the non-background phase [8], i.e.,

$$\lambda = \frac{\sum_{i=1}^{m} n_\mathrm{c}^{(i)}}{\eta^2 \sum_{i=1}^{m} \#\{x \in W \colon S^{(i)}(x) > 0\}}, \tag{12}$$

where $\eta = 14.3\,\mathrm{nm}$ denotes the pixel size.

2.4.2 Size and shape of individual cracks

In this section, further morphological descriptors for the characterization of individual cracks are described, which provide a more detailed view onto the structural degradation of cathode materials than the previously considered aggregated descriptors [8]. Such less aggregated descriptors can be computed for each crack $C \subset W$ observed in crack-wise segmentations, see Figure 1(bottom row, center), i.e., we obtain a sample of such crack descriptors for each degradation scenario, allowing us to compare the distributions of these descriptors in Section 3 below.

First, we consider the area-equivalent diameter d which characterizes the size of the crack C and is given by

$$d = 2\eta \sqrt{\frac{\#C}{\pi}}. \tag{13}$$

This descriptor is the diameter of a disk which has the same area as C. Since each segmented crack C is associated with a discretized curve $L \subset W$ which has been determined by skeletonizing the crack phase, see Section 2.3.2, we

define the crack length ℓ as the length of the curve L, i.e., we put

$$\ell = \eta \, \# L. \tag{14}$$

Moreover, we use the discretized curve L to compute a crack descriptor which characterizes the width of C. Namely, for each pixel $x \in L$, we can determine the maximum radius $r_{\mathrm{disk}}(x)$ of a circular disk centered at x such that the disk is fully contained by the crack phase, i.e.,

$$r_{\mathrm{disk}}(x) = \min\{\|x - y\| \colon y \in W, S(y) < 2\}. \tag{15}$$

Consequently, the width of the crack at $x \in L$ can be considered to be equal to $2r_{\mathrm{disk}}(x)$ and, by averaging these local crack widths, we obtain the crack width b given by

$$b = \frac{\eta}{\# L} \sum_{x \in L} 2r_{\mathrm{disk}}(x). \tag{16}$$

We compute the descriptor vector (d, ℓ, b) for each crack observed within the crack-wise segmentations $S_{\mathrm{c}}^{(1)}, \ldots, S_{\mathrm{c}}^{(m)}$ such that we obtain a sample $\mathcal{X}_{20}$ of crack descriptor vectors for cathodes cycled at 20 °C which has the form

$$\mathcal{X}_{20} = \left((d^{(i)}, \ell^{(i)}, b^{(i)}) \right)_{i=1}^{n_{20}}, \tag{17}$$

where $n_{20} > 0$ denotes the total number of cracks observed in $S_{\mathrm{c}}^{(1)}, \ldots, S_{\mathrm{c}}^{(m)}$. Note that we disregard descriptor vectors (d, ℓ, b) with a crack size d smaller than 2.5η, such that the descriptor vectors of small regions $C \subset W$ which are indistinguishable from noise are not included.

2.4.3 Analysis of crack growth

During structural degradation cracks do not only grow, but also new, smaller cracks are formed. In order to investigate crack growth, we consider large cracks separately. For that purpose, we determine an adjusted version of the dataset $\mathcal{X}_{20}$ which consists of descriptor vectors associated with large cracks. More precisely, the total area A_{20} of the non-background phase is given by

$$A_{20} = \frac{n_{20}}{\lambda}. \tag{18}$$

The number n_{pristine} of cracks that would appear in image data of pristine cathodes depicting the same total area of the non-background phase is given by

$$n_{\mathrm{pristine}} = \lfloor A_{20} \lambda_{\mathrm{pristine}} \rfloor, \tag{19}$$

where $\lambda_{\mathrm{pristine}} = 0.145 \, \mu\mathrm{m}^{-2}$ is the crack intensity observed in pristine cathodes [8] and $\lfloor \cdot \rfloor$ denotes the floor function, to ensure that n_{pristine} is an integer. Then, we obtain the adjusted dataset $\widetilde{\mathcal{X}}_{20}$ by disregarding the n_{pristine} descriptor vectors with the smallest crack sizes.

2.4.4 Porosity and specific surface area of individual particles

Instead of characterizing individual cracks as stated in Section 2.4.2, we now focus on descriptors which characterize individual particles $P \subset W$ observed in a particle-wise segmentation S_{p}. Recall that in Section 2.4.1 we introduced the global particle porosity ρ which characterizes the overall amount of cracks within the cathode particles. However, note that ρ is an aggregated quantity. Using the particle-wise segmentation S_{p} together with the corresponding phase-wise segmentation S, we can compute a porosity value $\rho_{\mathrm{p}} \in [0, 1]$ for each segmented particle $P \subset W$. This allows us to investigate the probability distribution of individual particle porosities. More precisely, the porosity ρ_{p} of a particle $P \subset W$ is given by

$$\rho_{\mathrm{p}} = \frac{\#\{x \in P \colon S(x) = 2\}}{\#\{x \in P \colon S(x) > 0\}}. \tag{20}$$

Another quantity, which characterizes the crack phase within individual particles is the specific surface area a of the solid phase of particles which can be estimated from the observed cross-section $P \subset W$ by considering the fraction of the perimeter of the solid phase in the cross-section $P \subset W$ divided by its area, i.e., we put

$$a = \frac{4}{\pi} \frac{\eta \operatorname{perim}(\{x \in P \colon S(x) = 1\})}{\eta^2 \, \#P}, \tag{21}$$

where $\operatorname{perim}(\cdot)$ denotes the perimeter which we compute using the `regionprops` function of the Python package scikit-image [37]. Note that the prefactor $\frac{4}{\pi}$ in Equation (21) corrects, under certain assumptions, the bias of estimating the specific surface area from planar sections [13, 15].

We determine the descriptor vector (ρ_p, a) for each particle observed within the particle-wise segmentations $S_\mathrm{p}^{(1)}, \ldots, S_\mathrm{p}^{(m)}$ such that we obtain a sample $\mathcal{Z}_{20}$ of particle descriptor vectors for cathodes cycled at 20 °C which has the form

$$\mathcal{Z}_{20} = \left((\rho_\mathrm{p}^{(i)}, a^{(i)}) \right)_{i=1}^{m_{20}}, \tag{22}$$

where $m_{20} > 0$ denotes the total number of particles observed in $S_\mathrm{p}^{(1)}, \ldots, S_\mathrm{p}^{(m)}$.

2.5 Local particle porosity

We now introduce morphological descriptors which characterize the local porosity of individual particles as a function of the distance to the particle center. However, since we observe only planar cross-sections of cathode particles, the distance of a pixel $x \in P$ within a particle cross-section $P \subset W$ to the actual particle center is unknown, see Figure 5. In particular, as indicated in Figure 5, from planar sections we can identify the cross-section radius $\tilde{r}$ and the distance d_b of a pixel $x \in P$ to the cross-section center. Then, the distance d to the particle center is given by

$$d(r) = \sqrt{r^2 - \tilde{r}^2 + d_\mathrm{b}^2}, \tag{23}$$

where the particle's radius r is unknown. In particular, this makes it difficult to investigate the porosity as a function of the normalized distance $d(r)/r \in [0, 1]$.

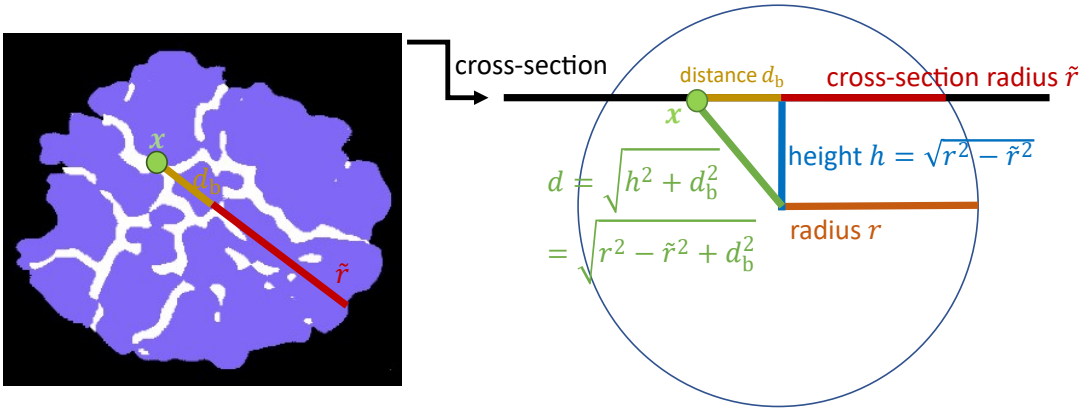

Figure 5: Distance to particle center from planar cross-sections. Left: Planar section through a particle P (solid phase in purple and crack phase in white) with cross-section radius $\tilde{r}$. For some pixel $x \in P$ we can determine only the distance d_b to the cross-section center and not the distance d to the particle center. Right: For spherical particles, this distance d can be determined when the particle's radius r is known.

Nevertheless, we show that it is possible to determine an estimate for the normalized distance $d(r)/r$ when the conditional distribution of the particle radii r is known, under the condition that the cross-section radius $\tilde{r}$ is given. Note that we can derive an estimate for $d(r)/r$ by considering its expected value under this conditional distribution. Therefore, we perform the following three steps: (i) We provide the definition of this conditional distribution for spherical particles and the resulting estimate for $d(r)/r$. (ii) We describe how this distribution is determined for the particles considered in the present paper to derive our estimator for the normalized distance of a pixel $x \in P$ to the particle center. (iii) We define the functional descriptor for the local particle porosity.

2.5.1 Conditional probability density of sphere radius

Let R be a random variable with some probability density $f_R\colon \mathbb{R} \to [0,\infty)$ which describes the random radius of a system of spherical particles. Furthermore, let $\widetilde{R}$ denote the random radius of a planar cross-section through a sphere with radius R which is observed when a plane is placed at a random height (i.e., parallel to the xy-plane) through the sphere. One can show that, under certain conditions, the conditional probability density $f_{\widetilde{R}|R=r}\colon \mathbb{R} \to [0,\infty)$ of the cross-section radius for a given sphere radius $r > 0$ is given by

$$f_{\widetilde{R}|R=r}(\widetilde{r}) = \begin{cases} \dfrac{\widetilde{r}}{r\sqrt{r^2-\widetilde{r}^2}}, & \text{if } 0 < \widetilde{r} \leq r, \\ 0, & \text{else,} \end{cases} \tag{24}$$

for each $\widetilde{r} \in \mathbb{R}$ [14]. Thus, the joint probability density $f_{(R,\widetilde{R})}\colon \mathbb{R}^2 \to [0,\infty)$ of R and $\widetilde{R}$ is given by

$$f_{(R,\widetilde{R})}(r,\widetilde{r}) = \begin{cases} f_R(r)\dfrac{\widetilde{r}}{r\sqrt{r^2-\widetilde{r}^2}}, & \text{if } 0 \leq \widetilde{r} < r, \\ 0, & \text{else.} \end{cases} \tag{25}$$

Consequently, for any given cross-section radius $\widetilde{r} > 0$, we can determine the conditional probability density $f_{R|\widetilde{R}=\widetilde{r}}\colon \mathbb{R} \to [0,\infty)$ of the particle radius using the fact that

$$f_{R|\widetilde{R}=\widetilde{r}}(r) = \frac{f_{(R,\widetilde{R})}(r,\widetilde{r})}{f_{\widetilde{R}}(\widetilde{r})}, \qquad \text{for each } r \geq 0, \tag{26}$$

where $f_{\widetilde{R}}\colon \mathbb{R} \to [0,\infty)$ denotes the (marginal) probability density of $\widetilde{R}$ given by

$$f_{\widetilde{R}}(\widetilde{r}) = \int_{-\infty}^{\infty} f_{(R,\widetilde{R})}(r,\widetilde{r})\,\mathrm{d}r, \qquad \text{for each } \widetilde{r} \geq 0. \tag{27}$$

The conditional probability density $f_{R|\widetilde{R}=\widetilde{r}}$ can be leveraged to estimate the distance of a point $x = (x_1, x_2, x_3) \in \mathbb{R}^3$ within the planar cross-section of a sphere to its center. For that purpose, we can assume that the sphere is centered at the origin $o = (0,0,0)$. Then, since the planar cross-section at the random height x_3 has the random radius $\widetilde{R}$, we get that $x_3^2 + \widetilde{R}^2 = R^2$ or, equivalently, $x_3 = \sqrt{R^2 - \widetilde{R}^2}$. Furthermore, let $d_{\mathrm{b}} = \sqrt{x_1^2 + x_2^2}$ denote the distance of x to the center $(0,0,x_3)$ of the planar cross-section of the sphere. This implies that the random distance $\widetilde{D}_{\mathrm{center}}(x)$ of x to the sphere center is given by

$$\widetilde{D}_{\mathrm{center}}(x) = \sqrt{x_3^2 + d_{\mathrm{b}}^2} = \sqrt{R^2 - \widetilde{R}^2 + d_{\mathrm{b}}^2}. \tag{28}$$

As spheres can have different radii, we consider a normalized version of the distance with respect to the sphere radius, i.e., the relative distance $D_{\mathrm{center}}(x)$ of x to the sphere center is given by

$$D_{\mathrm{center}}(x) = \frac{\widetilde{D}_{\mathrm{center}}(x)}{R}. \tag{29}$$

Thus, if the sphere radius is unknown and only a realization $\widetilde{r}$ of the random cross-section radius $\widetilde{R}$ is observed, we can compute an estimate $d_{\mathrm{center}}(x)$ for the relative distance $D_{\mathrm{center}}(x)$ by considering the conditional expectation, i.e.,

$$d_{\mathrm{center}}(x) = \mathbb{E}\big(D_{\mathrm{center}}(x) \mid \widetilde{R} = \widetilde{r}\big) = \int_{-\infty}^{\infty} \frac{1}{r}\sqrt{r^2 - \widetilde{r}^2 + d_{\mathrm{b}}^2}\; f_{R|\widetilde{R}=\widetilde{r}}(r)\,\mathrm{d}r. \tag{30}$$

2.5.2 Estimating the distance to the particle center

Since cathode particles have almost spherical shapes we apply Equation (30) to estimate the distance of a pixel $x \in P$ associated with a particle cross-section $P \subset W$ to the particle center. First, we have to determine the probability

density f_R of the particle radius. Some characteristics determined by means of laser-diffraction measurements of the particle size distribution of the NMC532 powders were provided by the manufacturer. More precisely, the values for the 10 %, 50 % and 90 % percentiles of the volume-weighted particle radius distributions[1] are given by $r_{10} = 3.55\,\mu\text{m}, r_{50} = 4.65\,\mu\text{m}$ and $r_{90} = 6.05\,\mu\text{m}$. In order to determine f_R, we fit the parameters $\mu \in \mathbb{R}$ and $\sigma > 0$ of a log-normal distribution, the probability density of which is given by

$$f(r;\mu,\sigma) = \begin{cases} \dfrac{1}{\sigma r\sqrt{2\pi}} \exp\left(-\dfrac{(\log(r)-\mu)^2}{2\sigma^2}\right), & \text{if } r > 0, \\ 0, & \text{else,} \end{cases} \tag{31}$$

to the percentiles stated above. For that purpose, we determine optimal parameters $\widehat{\mu}, \widehat{\sigma}$ by solving the minimization problem

$$(\widehat{\mu}, \widehat{\sigma}) = \operatorname*{arg\,min}_{\mu\in\mathbb{R},\sigma>0} \sum_{\alpha\in\{10,50,90\}} (z(\alpha;\mu,\sigma) - r_\alpha)^2, \tag{32}$$

where $z(\alpha;\mu,\sigma)$ denotes the α-percentile of the log-normal distribution with parameters μ, σ. Thus, we obtain a fit for the volume-weighted probability density f_V of the particle size distribution by $f_\text{V}(r) = f(r;\widehat{\mu},\widehat{\sigma})$ for each $r \in \mathbb{R}$, where $\widehat{\mu} = 1.53, \widehat{\sigma} = 0.208$. Then, the probability density f_R is given by

$$f_R(r) = \begin{cases} \frac{1}{c} f_\text{V}(r)/r^3, & \text{if } r > 0, \\ 0, & \text{else,} \end{cases} \tag{33}$$

where the normalizing constant c is given by $c = \int_0^\infty f_\text{V}(r)/r^3\,\mathrm{d}r$.

For a segmented particle cross-section $P \subset W$, we approximate the radius $\widetilde{r}$ of the observed cross-section, by considering the area-equivalent radius, i.e., we set

$$\widetilde{r} = \eta\sqrt{\frac{\#P}{\pi}}. \tag{34}$$

Recall that η and $\#P$ in Equation (34) denote the pixel size and the cardinality of P, respectively. Thus, by means of Equations (25) and (26) we can determine the (conditional) particle radius distribution given the observed cross-section radius $\widetilde{r}$. Furthermore, for any pixel $x \in P$, we estimate the distance of x to the cross-section center by determining the distance to the barycenter of P, i.e., we set

$$d_\text{b} = \eta\,\|x - \frac{1}{\#P}\sum_{y\in P} y\|. \tag{35}$$

Thus, using Equation (30), we can determine the relative distance $d_\text{center}(x,P)$ of any pixel $x \in P$ to the particle center by

$$d_\text{center}(x,P) = \int_{-\infty}^{\infty} \frac{1}{r}\sqrt{r^2 - \widetilde{r}^2 + \eta\|x - \frac{1}{\#P}\sum_{y\in P} y\|^2}\, f_{R|\widetilde{R}=\widetilde{r}}(r)\,\mathrm{d}r, \tag{36}$$

where the integrals appearing in Equations (27) and (36) are computed numerically.

2.5.3 Computation of local particle porosity

Recall that $S^{(i)}$ denotes the phase-wise segmentation of the SEM image $I^{(i)}$, and $P_1^{(i)}, \ldots, P_{n_\text{p}^{(i)}}^{(i)} \subset W$ are the segmented particle cross-sections in the particle-wise segmentation $S_\text{p}^{(i)}$ of $I^{(i)}$ for $i = 1, \ldots, m$. In order to determine the local particle porosity as a function of distance to the particle center, we proceed in the following way. Let $a, b > 0$ be some real numbers with $a < b$. Then, for each for $i = 1, \ldots, m$, we compute the areas of the crack and solid phases in $I^{(i)}$, respectively, by counting the number of pixels $x \in P_1^{(i)} \cup \cdots \cup P_{n_\text{p}^{(i)}}^{(i)} \subset W$, whose relative distance

[1] If $f\colon \mathbb{R} \to [0,\infty)$ is the probability density of the particle size distribution, then the volume-weighted probability density $f_\text{V}\colon \mathbb{R} \to [0,\infty)$ is given by $f_\text{V}(r) = \frac{1}{c} r^3 f(r)$, where the normalizing constant c is given by $c = \int_0^\infty r^3 f(r)\,\mathrm{d}r$.

$d_{\text{center}}(x, P_j^{(i)})$ to the j-th particle center (corresponding to the cross-section $P_j^{(i)}$) belongs to the interval $[a, b)$ for some $j \in \{1, \ldots, n_{\text{p}}^{(i)}\}$. More precisely, the quantities $A_{\text{crack}}([a, b))$ and $A_{\text{particle}}([a, b))$ are determined, where

$$A_{\text{crack}}([a,b)) = \eta^2 \sum_{i=1}^{m} \sum_{j=1}^{n_{\text{p}}^{(i)}} \sum_{x \in P_j^{(i)}} \mathbb{1}_{[a,b)}\left(d_{\text{center}}(x, P_j^{(i)})\right) \mathbb{1}_{\{y \in W\colon S^{(i)}(y)=2\}}(x) \tag{37}$$

and

$$A_{\text{particle}}([a,b)) = \eta^2 \sum_{i=1}^{m} \sum_{j=1}^{n_{\text{p}}^{(i)}} \sum_{x \in P_j^{(i)}} \mathbb{1}_{[a,b)}\left(d_{\text{center}}(x, P_j^{(i)})\right) \mathbb{1}_{\{y \in W\colon S^{(i)}(y)=1\}}(x). \tag{38}$$

Here, for some set A, the indicator function $\mathbb{1}_B$ of some subset $B \subset A$ is the function $\mathbb{1}_B\colon A \to \{0, 1\}$ given by

$$\mathbb{1}_B(x) = \begin{cases} 1, & \text{if } x \in B, \\ 0, & \text{else.} \end{cases} \tag{39}$$

Finally, we determine the local porosity $\rho_{\text{local}}([a, b))$ corresponding to those pixels whose relative distance to a particle center belongs to $[a, b)$, i.e., we compute the quotient

$$\rho_{\text{local}}([a,b)) = \frac{A_{\text{crack}}([a,b))}{A_{\text{particle}}([a,b)) + A_{\text{crack}}([a,b))}. \tag{40}$$

Thus, by considering $\rho_{\text{local}}([a_1, a_2)), \rho_{\text{local}}([a_2, a_3)), \ldots, \rho_{\text{local}}([a_k - 1, a_k))$ for some $k > 0$ and $0 \leq a_1 < a_2 < \cdots < a_k$ we can characterize the local porosity as a function of distance to the particle center.

3 Results

In this section, we provide both results of the electrochemical analysis and the structural characterization of cracking in differently cycled cathodes (20 °C, 30 °C, 40 °C, 50 °C).

Aging modes, loss of lithium inventory (LLI) and loss of active material (LAM), were evaluated using incremental capacity (IC) analysis coupled with a deep learning (DL) model. Instead of the conventional IC method, which compares C/20 emulated IC curves with experimentally acquired IC curves individually by adjusting LLI and LAM, the synthetic data-based DL model quantified the aging modes quickly in an automated fashion. Synthetic IC data, including all possible scenarios, was generated to train the DL model, and the trained models quantified the aging modes at each RPT. The details of the IC-DL model are documented in a previous publication [38]. Results on the electrochemical performance of the cycled cathodes, including the capacity fade, the loss of positive electrode active material and the loss of Li inventory, are provided in Figure 6. The evolution of incremental capacity curves and the validation of estimated LLI at different temperatures are available in Figure S1.

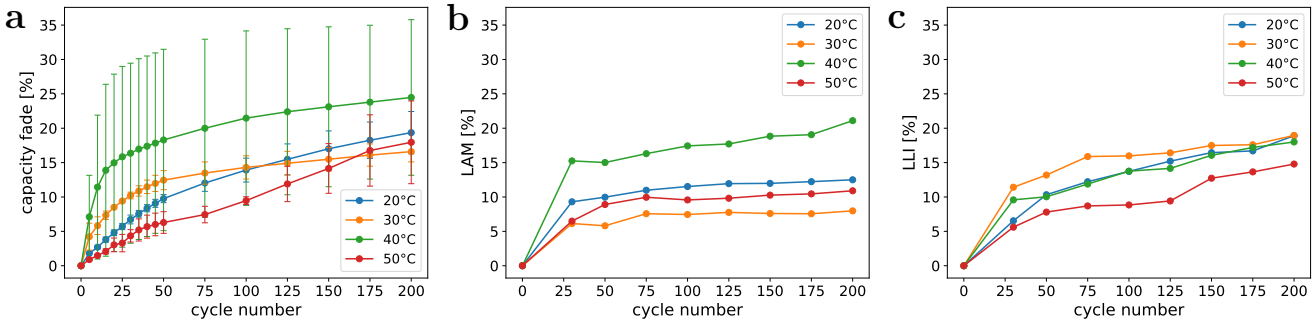

Figure 6: Electrochemical analysis. (a) Capacity fade, (b) loss of positive electrode active material, and (c) loss of Li inventory, versus cycle number. All data are based on C/20 capacity measurements. (b) and (c) are obtained from incremental capacity analysis.

Additionally, based on the descriptors introduced in Section 2.4 we performed a structural characterization of the considered cathodes. For example, from the SEM images acquired for cathodes cycled at 20 °C, we have determined a global particle porosity of $\rho = 0.0852$ by means of Equation (11) and a crack intensity of $\lambda = 0.241\,\mu\text{m}^{-2}$ by means of Equation (12). The corresponding global particle porosity and crack intensity values for cathodes cycled at 30 °C, 40 °C and 50 °C are listed in Table 1.

cycling condition	20 °C	30 °C	40 °C	50 °C
global particle porosity $[10^{-3}]$	34.3 ± 6.6	40.1 ± 5.1	39.5 ± 4.7	50.3 ± 8.6
crack intensity $[10^{-2} \cdot \mu\text{m}^{-2}]$	24.1 ± 2.3	30.0 ± 4.1	38.4 ± 3.5	36.9 ± 5.6

Table 1: Mean value and standard deviation of global particle porosity ρ and crack intensity λ for cathodes cycled at different cycling conditions.

In addition to such aggregated descriptors, in Section 2.4.2 we introduced descriptors for individual cracks. In particular, the dataset $\mathcal{X}_{20}$ consists of the crack sizes $d^{(1)}, \ldots, d^{(n_{20})}$. Thus, we can characterize the crack size distribution of cathodes cycled at 20 °C by investigating the boxplot of these crack size values, see Figure 7a—which also visualizes the corresponding boxplots of crack sizes determined for the other cycling conditions 30 °C, 40 °C and 50 °C. Analogously, Figures 7b and 7c visualize such boxplots of crack lengths and widths, respectively. Note that the numbers of observed cracks for the considered cycling conditions are given by $n_{20} = 8733, n_{30} = 11212, n_{40} = 17866, n_{50} = 21242$.

For analyzing the influence of operating temperature on the growth of existing cracks, we additionally determined such boxplots from adjusted datasets $\widetilde{\mathcal{X}}_j$ for $j \in \{20, 30, 40, 50\}$ for which we have omitted descriptor vectors with small crack sizes, where the structural characterization of pristine cathodes [8] has been chosen as a reference for determining the number of omitted descriptor vectors, see Figures 7d-f.

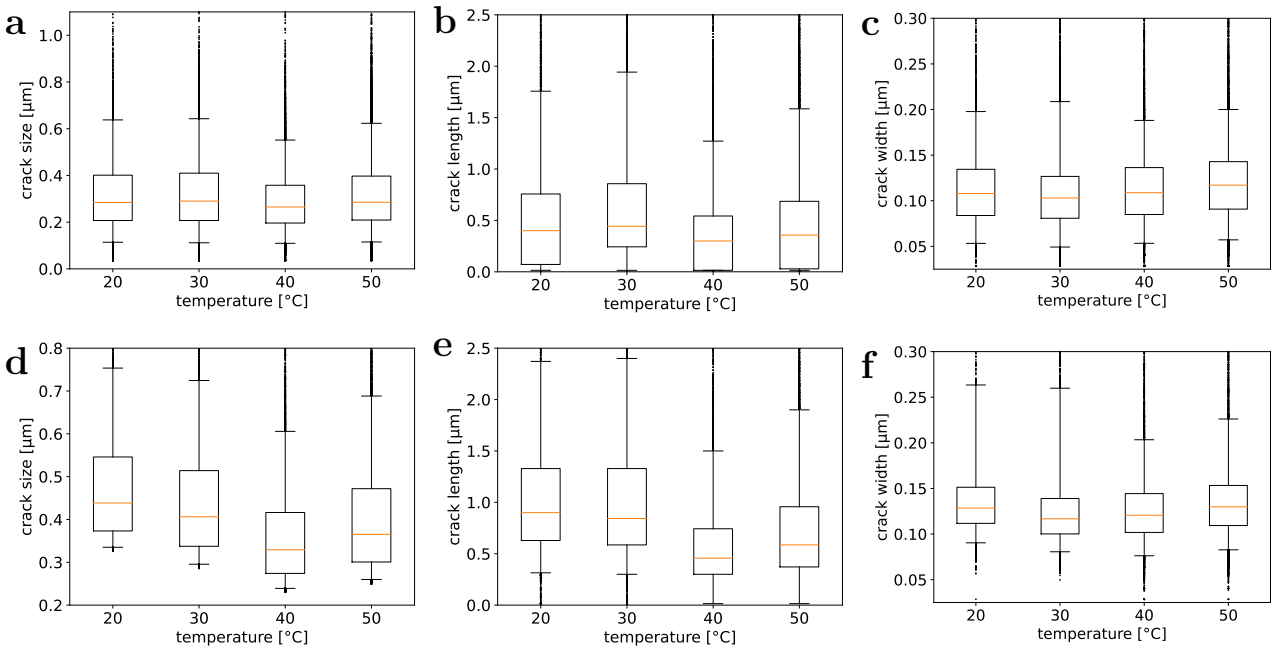

Figure 7: Boxplots of crack size (a), length (b) and width (c) computed from the datasets $\mathcal{X}_j$ for each cycling condition $j \in \{20, 30, 40, 50\}$. The bottom and top ends of the boxes indicate the first and third quartiles. Median values are represented by red lines within the boxes. The whiskers show the 5th and 95th percentiles, whereas points indicate outliers. The corresponding boxplots computed from the adjusted datasets $\widetilde{\mathcal{X}}_j$ for each cycling condition $j \in \{20, 30, 40, 50\}$ are visualized in (d)-(f).

In Section 2.4.4 we have introduced descriptors which characterize the cracks of individual particles, namely the particle porosity ρ_{p} and the specific surface area a. The corresponding boxplots of these descriptors are visualized in Figure 8 for all cycling conditions considered in the present paper.

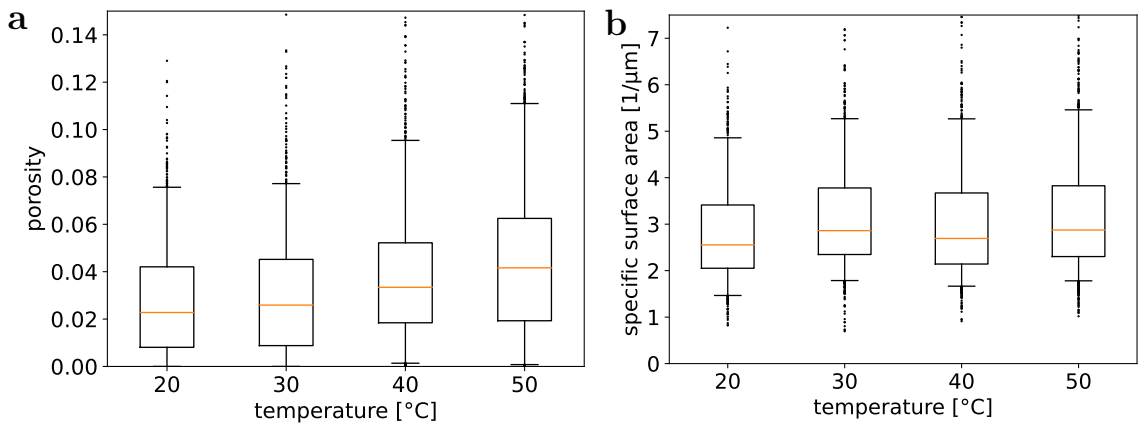

Figure 8: Boxplots of particle porosity (a) and specific surface area (b) computed from the datasets $\mathcal{Z}_j$ for each cycling condition $j \in \{20, 30, 40, 50\}$. The bottom and top ends of the boxes indicate the first and third quartiles. Median values are represented by red lines within the boxes. The whiskers show the 5th and 95th percentiles, whereas points indicate outliers.

To conclude the quantitative analysis of structural degradation, we consider the local porosity introduced in Section 2.5. This descriptor quantifies the particle porosity as a function of distance to the particle center. The corresponding results for all cycling conditions are visualized in Figure 9.

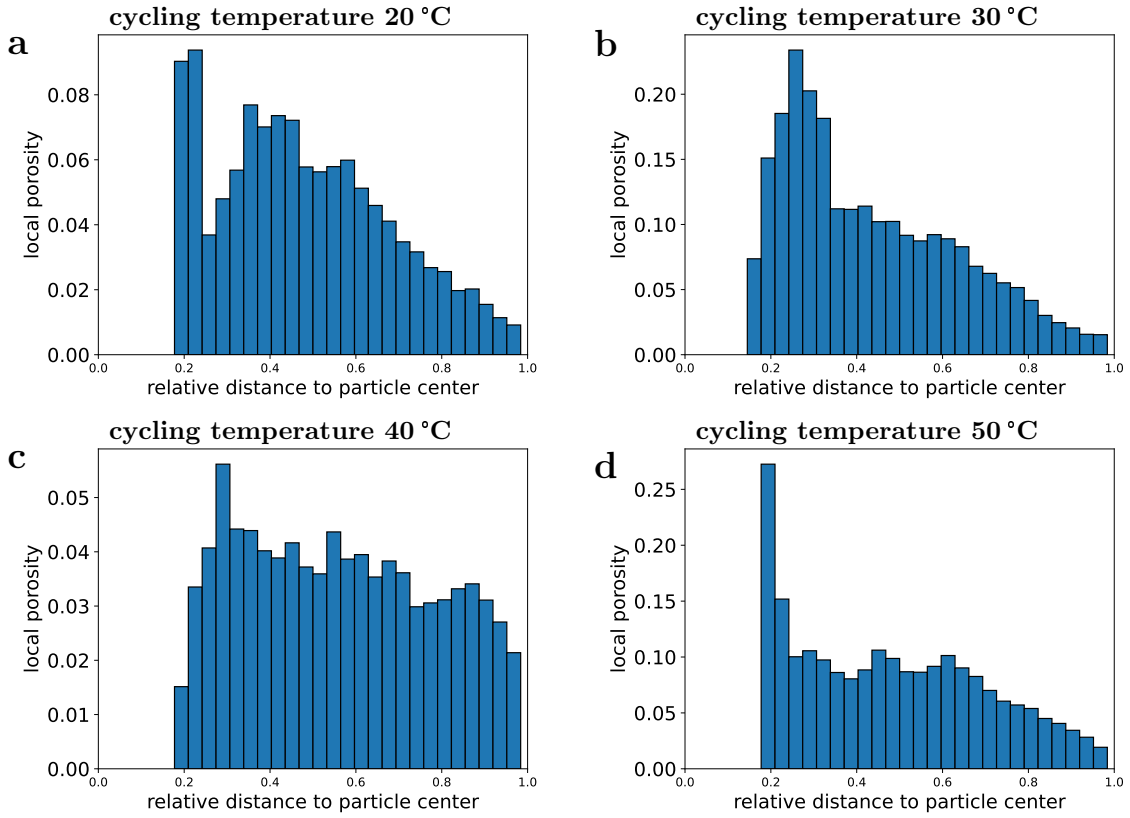

Figure 9: Local porosity as a function of distance to particle center for cathodes cycled at 20 °C (a), 30 °C (b), 40 °C (c) and 50 °C (d). Bin heights represent the local porosity value $\rho_{\text{local}}([a, b))$, where $a < b$ are the bin edges.

4 Discussion

As stated in [8] some of the considered structural descriptors might not be representative of the actual 3D degraded-cathode structure since some effects are not observable in 2D image data. For example, two non-connected cracks observed in cross-sectional data might actually be connected in 3D, thus there might be a systematic bias for the crack size distributions determined from 2D data. Nevertheless, such descriptors still allow for some quantitative structural comparison between the differently cycled cathode materials considered in the present paper. Moreover, the method described in Section 2.5 for the characterization of local particle porosities takes such discrepancies between 2D and 3D image data into account (under the assumption of spherical NMC particles). A possible approach which does not require this assumption could be as follows: By simulating a large number of virtual NMC particles [39] and their planar sections at random heights, we could determine d-dimensional morphological descriptor vectors $x_{\text{2D}} \in \mathbb{R}^d$ for the planar sections of particles [40]. Then, such morphological descriptor vectors could be correlated with the cut-height h of the planar section (i.e., the distance between the particle center and the planar section) by modeling the joint distribution of x_{2D} and h, e.g., using so-called copulas [6, 41]. Then, we can determine the conditional distribution of the cut height for a given descriptor vector x_{2D}—allowing us to infer the cut height h. In particular, from the cut height h we can determine the distance of a point within a planar section of a particle to its center. Subsequently, the method from Section 2.5 could be used analogously to determine the local porosity from planar sections for non-spherical particles.

Now, we discuss the influence of operating temperature on the degradation of cathodes based on the structural characterization given in Section 2.5. We observe that the global particle porosity increases monotonically with respect to the operating temperature, see Table 1. This monotonic influence of the temperature can also be observed on the distribution of the particle porosity, see Figure 8a. In contrast, the crack intensity only increases "mostly"

monotonically with the operating temperature, with the exception for the cycling condition of 40 °C, see Table 1. Moreover, as it can be seen in Figures 7a-c and Figure 8b the temperature does not seem to significantly influence crack size/length/width distributions as well as the distributions of specific particle surface area.

Interestingly, when considering the effect of crack growth, by considering only large cracks, see Section 2.4, we observe an overall decrease in crack width and length with increasing temperatures from both 20 °C to 30 °C as well as from 30 °C to 40 °C—however, an increase in crack width and length is observed from 40 °C to 50 °C, see Figure 7d,e. Similarly, when considering only large cracks, the crack width decreases first with increasing temperature, followed by a rise in crack widths, see Figure 7f. In Figure 9, we observe that the local porosity increases monotonically from the particle exterior to the particle center, again this observation is not as well pronounced for cathodes which have been cycled at 40 °C. The 40 °C data is an outlier for both the particle-damage and capacity-fade trends. Incremental capacity analysis (Figure 6) shows that the reason for abnormally high capacity fade in the 40 °C-aged cells is due to excessive loss of cathode active material. The reason for this is not understood. We omit the 40 °C data from our further discussion of damage trends with temperature.

We hypothesize two possible causes of increasing particle porosity with temperature. First, due to faster transport and kinetics, the elevated temperature cells had higher charge acceptance, experiencing higher ΔSOC swings with each cycle. The elevated temperature cells also experienced less capacity fade, thus sustaining the large ΔSOC through most of their lifetime. Larger ΔSOC swings at elevated temperature cause large volume changes that possibly increased the magnitude of particle fracture and porosity. The second possible cause of increased particle porosity at high temperature is due to a softening of mechanical properties with temperature. For example, tensile tests of a composite cathode showed a 25% reduction in max tensile stress and 55% decrease in fracture strain of a composite cathode between 20 °C and 80 °C [42]. We are unable to find in the literature temperature-dependent mechanical properties for the present NMC532 material. The softening of the binder and aluminum current collector no doubt played a role in this composite-electrode's temperature dependence. Nonetheless, the composite electrode structure determines the mechanical boundary conditions of individual particles and thus influences their damage state.

Figure 9 indicates that local porosity is greatest at the particle center. This observation is contrary to high C-rate charging of the full cell (rapid delithiation of cathode particles) which, for a homogeneous particle, is expected to result in more cracking in the exterior region of cathode particles [43]. For heterogeneous polycrystalline particles, the crack pattern is more complex [44]. Preferential cracking near the particle center could also be caused by high-rate discharge of the full cell, however the present cells were discharged at the relatively low C/2 rate. Additional reasons for preferential cracking observed near the particle center include stress/strain from the calendering step of manufacturing and stress/strain caused by the aforementioned or ΔSOC (bulk volume) changes, independent of fast-charge rate.

5 Conclusion

The structural degradation of lithium-ion positive electrodes cycled under various operating temperatures has been quantified from SEM images. For that purpose a generative adversarial network has been deployed to super-resolve the data, in order to improve the segmentation results. The structural characterization of segmented data included aggregated descriptors, such as global particle porosity as well as crack intensity, but also the distribution of various crack and particle descriptors. Additionally, using methods from stereology the local particle porosity has been computed as a function of distance to the particle center.

To obtain SEM images, full graphite/NMC532 cells were first cycled for 200 cycles at a C/2-discharge rate and a fast 6C-charge rate with a 4.1 V maximum voltage. The 4.1 V cell-level maximum limits the cathode maximum voltage to <4.2 V, avoiding large phase transitions known to cause more severe fade. Shown in our previous study for the same material [8], significant cracking exists already in pristine electrodes indicating that initial cracks are caused manufacturing processes. This paper shows that subsequent crack magnitude increases with temperature. Two hypothesized causes for this temperature dependence are (1) higher charge throughput and ΔSOC window experienced by the high temperature fast-charge-aged cells and (2) softening of mechanical properties at high temperature.

While SEM images were only available from post-mortem teardowns after 200 cycles, incremental capacity analysis (Figure 6, SI) provided cycling-resolved diagnostics showing loss of Li inventory dominated cell-level capacity

fade. Nonetheless, loss of cathode active material was also substantial, representing a hidden mechanism known to cause late-life impedance rise and accelerated capacity fade. By quantifying the magnitude of particle cracking versus cycling condition (previous work, [8]) and temperature (this work), future work will more deeply validate 3D electrochemo-mechanical damage models of nickelate cathodes [3], providing a means to optimize cathode material architecture for long life and fast-charge capability.

Data availability

The datasets generated during and/or analysed during the current study are available from the corresponding authors on reasonable request.

Code availability

All formulations and algorithms necessary to reproduce the results of this study are described in the Results and Methods sections.

Acknowledgements

This work was authored in part by the National Renewable Energy Laboratory, operated by Alliance for Sustainable Energy, LLC, for the U.S. Department of Energy (DOE) under Contract No. DE-AC36-08GO28308 and the Battelle Energy Alliance, LLC, under Contract No. DE- AC07-05ID14517 for Idaho National Laboratory with the U.S. DOE. Funding was provided by the U.S. DOE Office of Vehicle Technology Extreme Fast Charge Program, program manager Brian Cunningham. The views expressed in the article do not necessarily represent the views of the DOE or the U.S. Government. The U.S. Government retains and the publisher, by accepting the article for publication, acknowledges that the U.S. Government retains a nonexclusive, paid-up, irrevocable, worldwide license to publish or reproduce the published form of this work, or allow others to do so, for U.S. Government purposes. The work of MN was funded by DFG under Project ID 390874152 (POLiS Cluster of Excellence, EXC 2154). The present paper contributes to the research performed at CELEST (Center for Electrochemical Energy Storage Ulm-Karlsruhe). The authors acknowledge the support from Argonne National Laboratory, which is a U.S. DOE Office of Science Laboratory operated by UChicago Argonne, LLC, under Contract No. DE-AC02–06CH11357.

Author contributions

Elecrochemical data on cycled cathodes was acquired by S.K. and T.R.T. SEM measurements were performed by Z.Y. Processing and statistical analysis of image data was performed by O.F. Main parts of the paper were written by D.P.F., O.F., K.S., T.R.T., P.W. and Z.Y. The methodology described in Section 2.5 has been derived by O.F. and M.N. All authors discussed the results and contributed to writing of the manuscript. K.S. and V.S. designed and supervised the research.

Competing interests

The authors declare no competing financial or non-financial interests.

References

[1] T. R. Tanim, Z. Yang, D. P. Finegan, Y. L. Parameswara R. Chinnam, P. J. Weddle, I. Bloom, A. M. Colclasure, E. J. Dufek, Y. T. Jianguo Wen, M. C. Evans, K. Smith, J. M. Allen, A. H. Q. Charles C. Dickerson, A. R.

Dunlop, S. E. Trask, A. N. Jansen, A comprehensive understanding of the aging effects of extreme fast charging on high Ni NMC cathode, Advanced Energy Materials 12 (2022) 2103712. doi:DOI:10.1002/aenm.202103712.

[2] T. R. Tanim, Z. Yang, A. M. Colclasure, P. R. Chinnam, P. Gasper, Y. Lin, L. Yu, P. J. Weddle, J. Wen, E. J. Dufek, I. Bloom, K. Smith, C. C. Dickerson, M. C. Evans, Y. Tsai, A. R. Dunlop, S. E. Trask, B. J. Polzin, A. N. Jansen, Extended cycle life implications of fast charging for lithium-ion battery cathode, Energy Storage Materials 41 (2021) 656–666. doi:10.1016/j.ensm.2021.07.001.

[3] J. M. Allen, P. J. Weddle, A. Verma, A. Mallarapu, F. Usseglio-Viretta, D. P. Finegan, A. M. Colclasure, W. Mai, V. Schmidt, O. Furat, D. Diercks, T. Tanim, K. Smith, Quantifying the influence of charge rate and cathode-particle architectures on degradation of Li-ion cells through 3D continuum-level damage models, Journal of Power Sources 512 (2021) 230415. doi:10.1016/j.jpowsour.2021.230415.

[4] O. Furat, D. P. Finegan, D. Diercks, F. Usseglio-Viretta, K. Smith, V. Schmidt, Mapping the architecture of single electrode particles in 3D, using electron backscatter diffraction and machine learning segmentation, Journal of Power Sources 483 (2021) 229148. doi:10.1016/j.jpowsour.2020.229148.

[5] H. Michael, F. Iacoviello, T. M. M. Heenan, A. Llewellyn, J. S. Weaving, R. Jervis, D. J. L. Brett, P. R. Shearing, A dilatometric study of graphite electrodes during cycling with X-ray computed tomography, Journal of The Electrochemical Society 168 (2021) 010507. doi:10.1149/1945-7111/abd648.

[6] O. Furat, T. Leißner, K. Bachmann, J. Gutzmer, U. Peuker, V. Schmidt, Stochastic modeling of multidimensional particle properties using parametric copulas, Microscopy and Microanalysis 25 (2019) 720–734. doi:10.1017/S1431927619000321.

[7] M. Neumann, A. Wagner, N. Bohn, M. Osenberg, A. Hilger, I. Manke, J. R. Binder, V. Schmidt, Characterization of hierarchically structured electrodes with different thicknesses by means of experiments and image analysis, Materials Characterization 155 (2019) 109778. doi:10.1016/j.matchar.2019.06.020.

[8] O. Furat, D. P. Finegan, Z. Yang, T. Tanim, K. Smith, V. Schmidt, Quantifying the impact of charge rate and number of cycles on structural degeneration of Li-ion battery electrodes, Journal of The Electrochemical Society 169 (2022) 100541. doi:10.1149/1945-7111/ac99a1.

[9] B. Prifling, M. Röding, P. Townsend, M. Neumann, V. Schmidt, Large-scale statistical learning for mass transport prediction in porous materials using 90,000 artificially generated microstructures, Frontiers in Materials 8 (2021) 786502. doi:10.3389/fmats.2021.786502.

[10] B. Prifling, M. Neumann, S. Hein, T. Danner, E. Heider, A. Hoffmann, P. Rieder, A. Hilger, M. Osenberg, I. Manke, M. Wohlfahrt-Mehrens, A. Latz, V. Schmidt, Quantitative comparison of different approaches for reconstructing the carbon-binder domain from tomographic image data of cathodes in lithium-ion batteries and its influence on electrochemical properties, Energy Technology 10 (2022) 2200784. doi:10.1002/ente.202200784.

[11] S. D. Wicksell, The corpuscle problem. A mathematical study of a biometric problem, Biometrika 17 (1-2) (1925) 84–99. doi:10.1093/biomet/17.1-2.84.

[12] S. D. Wicksell, The corpuscle problem: Second memoir: Case of ellipsoidal corpuscles, Biometrika 18 (1926) 151–172. doi:10.2307/2332500.

[13] S. N. Chiu, D. Stoyan, W. S. Kendall, J. Mecke, Stochastic Geometry and Its Applications, J. Wiley & Sons, 2013.

[14] A. Baddeley, E. B. V. Jensen, Stereology for Statisticians, Chapman and Hall/CRC, 2004.

[15] R. Schneider, W. Weil, Stochastic and Integral Geometry, Springer, 2008.

[16] L.-M. C. Orive, Particle size-shape distributions: The general spheroid problem, Journal of Microscopy 107 (3) (1976) 235–253. doi:10.1111/j.1365-2818.1976.tb02446.x.

[17] L.-M. C. Orive, Particle size-shape distributions: The general spheroid problem: II. Stochastic model and practical guide, Journal of Microscopy 112 (2) (1978) 153–167. doi:10.1111/j.1365-2818.1978.tb01162.x.

[18] A. Hobolth, The spherical deformation model, Biostatistics 4 (4) (2003) 583–595. doi:10.1093/biostatistics/4.4.583.

[19] J. F. Ziegel, J. R. Nyengaard, E. B. Vedel Jensen, Estimating particle shape and orientation using volume tensors, Scandinavian Journal of Statistics 42 (3) (2015) 813–831. doi:10.1111/sjos.12138.

[20] T. Ueda, Estimation of three-dimensional particle size and shape characteristics using a modified 2D–3D conversion method employing spherical harmonic-based principal component analysis, Powder Technology 404 (2022) 117461. doi:10.1016/j.powtec.2022.117461.

[21] T. Ueda, T. Oki, S. Koyanaka, Stereological bias for spherical particles with various particle compositions, Advanced Powder Technology 27 (4) (2016) 1828–1838. doi:10.1016/j.apt.2016.06.016.

[22] O. O. Taiwo, D. P. Finegan, D. S. Eastwood, J. L. Fife, L. D. Brown, J. A. Darr, P. D. Lee, D. J. Brett, P. R. Shearing, Comparison of three-dimensional analysis and stereological techniques for quantifying lithium-ion battery electrode microstructures, Journal of Microscopy 263 (3) (2016) 280–292. doi:10.1016/j.powtec.2022.117461.

[23] J. Fu, D. Xiao, D. Li, H. R. Thomas, C. Li, Stochastic reconstruction of 3D microstructures from 2D cross-sectional images using machine learning-based characterization, Computer Methods in Applied Mechanics and Engineering 390 (2022) 114532. doi:10.1016/j.cma.2021.114532.

[24] S. Kench, S. J. Cooper, Generating three-dimensional structures from a two-dimensional slice with generative adversarial network-based dimensionality expansion, Nature Machine Intelligence 3 (4) (2021) 299–305.

[25] M. Neumann, P. Gräfensteiner, C. Santos de Oliveira, J. Martins de Souza e Silva, S. Koppka, D. Enke, P. Huber, V. Schmidt, The morphology of nanoporous glass: Stochastic 3d modeling, stereology and the influence of pore width, Available at SSRN: https://ssrn.com/abstract=4414642, doi:10.2139/ssrn.4414642.

[26] F. Tian, L. Ben, H. Yu, H. Ji, W. Zhao, Z. liu, R. Monteiro, R. M. Ribas, Y. Zhu, X. Huang, Understanding high-temperature cycling-induced crack evolution and associated atomic-scale structure in a Ni-rich $LiNi_{0.8}Co_{0.1}Mn_{0.1}O_2$ layered cathode material, Nano Energy 98 (2022) 107222. doi:10.1016/j.nanoen.2022.107222.

[27] O. Furat, D. P. Finegan, D. Diercks, T. Kirstein, K. Smith, V. Schmidt, Super-resolving microscopy images of Li-ion electrodes for fine-feature quantification using generative adversarial networks, npj Computational Materials 8 (2022) 68. doi:10.1038/s41524-022-00749-z.

[28] D. C. Robertson, L. Flores, A. R. Dunlop, S. E. Trask, F. L. E. Usseglio-Viretta, A. M. Colclasure, Z. Yang, I. Bloom, Effect of anode porosity and temperature on the performance and lithium plating during fast-charging of lithium-ion cells, Energy Technology 9 (2021) 2000666. doi:10.1002/ente.202000666.

[29] C. Ledig, L. Theis, F. Huszár, J. Caballero, A. Cunningham, A. Acosta, A. Aitken, A. Tejani, J. Totz, Z. Wang, W. Shi, Photo-realistic single image super-resolution using a generative adversarial network, in: Proceedings of the IEEE Conference on Computer Vision and Pattern Recognition, IEEE Computer Society, Honolulu, HI, USA, 2017, pp. 105–114. doi:10.1109/CVPR.2017.19.

[30] S. Liu, W. Deng, Very deep convolutional neural network based image classification using small training sample size, in: Proceedings of the 3rd IAPR Asian Conference on Pattern Recognition, Kuala Lumpur, Malaysia, 2015, pp. 730–734. doi:10.1109/ACPR.2015.7486599.

[31] M. Abadi, A. Agarwal, P. Barham, E. Brevdo, Z. Chen, C. Citro, G. S. Corrado, A. Davis, J. Dean, M. Devin, S. Ghemawat, I. Goodfellow, A. Harp, G. Irving, M. Isard, Y. Jia, R. Jozefowicz, L. Kaiser, M. Kudlur, J. Levenberg, D. Mané, R. Monga, S. Moore, D. Murray, C. Olah, M. Schuster, J. Shlens, B. Steiner, I. Sutskever, K. Talwar, P. Tucker, V. Vanhoucke, V. Vasudevan, F. Viégas, O. Vinyals, P. Warden, M. Wattenberg, M. Wicke, Y. Yu, X. Zheng, TensorFlow: Large-scale machine learning on heterogeneous systems, software available from https://www.tensorflow.org (2015).

[32] D. P. Kingma, J. Ba, Adam: A method for stochastic optimization, in: Y. Bengio, Y. LeCun (Eds.), Proceedings of the 3rd International Conference on Learning Representations, ICLR, San Diego, CA, USA, 2015.

[33] J. P. Bertoldo, E. Decencière, D. Ryckelynck, H. Proudhon, A modular U-Net for automated segmentation of X-ray tomography images in composite materials, Frontiers in Materials 8 (2021) 493. doi:10.3389/fmats.2021.761229.

[34] O. Ronneberger, P. Fischer, T. Brox, U-Net: Convolutional networks for biomedical image segmentation, in: N. Navab, J. Hornegger, W. M. Wells, A. F. Frangi (Eds.), Proceedings of Medical Image Computing and Computer-Assisted Intervention, Springer, Cham, Switzerland, 2015, pp. 234–241. doi:10.1007/978-3-319-24574-4_28.

[35] T. Lee, R. Kashyap, C. Chu, Building skeleton models via 3-D medial surface axis thinning algorithms, CVGIP: Graphical Models and Image Processing 56 (1994) 462–478. doi:10.1006/cgip.1994.1042.

[36] J. B. T. M. Roerdink, A. Meijster, The watershed transform: Definitions, algorithms and parallelization strategies, Fundamenta Informaticae 41 (2000) 187–228. doi:10.3233/FI-2000-411207.

[37] S. van der Walt, J. L. Schönberger, J. Nunez-Iglesias, F. Boulogne, J. D. Warner, N. Yager, E. Gouillart, T. Yu, the scikit-image contributors, scikit-image: Image processing in Python, PeerJ 2 (2014) e453. doi:10.7717/peerj.453.

[38] S. Kim, Z. Yi, B.-R. Chen, T. R. Tanim, E. J. Dufek, Rapid failure mode classification and quantification in batteries: A deep learning modeling framework, Energy Storage Materials 45 (2022) 1002–1011. doi:10.1016/j.ensm.2021.07.016.

[39] O. Furat, J. Petrich, D. P. Finegan, D. Diercks, F. Usseglio-Viretta, K. Smith, V. Schmidt, Artificial generation of representative single Li-ion electrode particle architectures from microscopy data, npj Computational Materials 7 (2021) 105. doi:10.1038/s41524-021-00567-9.

[40] O. Furat, T. Leißner, R. Ditscherlein, O. Šedivý, M. Weber, K. Bachmann, J. Gutzmer, U. Peuker, V. Schmidt, Description of ore particles from X-ray microtomography (XMT) images, supported by scanning electron microscope (SEM)-based image analysis, Microscopy and Microanalysis 24 (5) (2018) 461–470. doi:10.1017/S1431927618015076.

[41] C. Czado, Analyzing Dependent Data with Vine Copulas, Springer, 2019.

[42] J. Kim, A. Mallarapu, S. Santhanagopalan, Abuse response of batteries subjected to mechanical impact, in: S. Santhanagopalan (Ed.), Computer Aided Engineering of Batteries. Modern Aspects of Electrochemistry, Springer, 2023, pp. 199–242. doi:10.1007/978-3-031-17607-4_6.

[43] J. Christensen, J. Newman, A mathematical model of stress generation and fracture in lithium manganese oxide, Journal of The Electrochemical Society 153 (2006) A1019. doi:10.1149/1.2185287.

[44] Y. Zhao, P. Stein, Y. Bai, M. Al-Siraj, Y. Yang, B.-X. Xu, A review on modeling electro-chemo-mechanics in lithium-ion batteries, Journal of Power Sources 413 (2019) 259–283. doi:10.1149/1.2185287.